ELSEVIER

Contents lists available at ScienceDirect

# Intermetallics

journal homepage: www.elsevier.com/locate/intermet





# Design and properties of novel Ti–Zr–Hf–Nb–Ta high-entropy alloys for biomedical applications

Wei Yang <sup>a</sup>, Shujie Pang <sup>a,b,\*</sup>, Ying Liu <sup>c</sup>, Qing Wang <sup>d</sup>, Peter K. Liaw <sup>e</sup>, Tao Zhang <sup>a,\*\*</sup>

- <sup>a</sup> Key Laboratory of Aerospace Materials and Performance (Ministry of Education), School of Materials Science and Engineering, Beihang University, Beijing, 100191, China
- <sup>b</sup> Beijing Advanced Innovation Center for Biomedical Engineering, Beihang University, Beijing, 100191, China
- <sup>c</sup> AVIC Manufacturing Technology Institute, Beijing, 100024, China
- d Key Laboratory of Materials Modification By Laser, Ion and Electron Beams (Ministry of Education), School of Materials Science and Engineering, Dalian University of Technology, Dalian, 116024, China
- <sup>e</sup> Department of Materials Science and Engineering, The University of Tennessee, Knoxville, TN, 37996, USA

#### ARTICLE INFO

# Keywords: High-entropy alloys Alloy design Biocompatibility Corrosion Mechanical properties Microstructure

#### ABSTRACT

The novel high-entropy alloys (HEAs) with compositions of  $(Ti_{1/3}Zr_{1/3}Hf_{1/3})_{15}(Nb_{1/2}Ta_{1/2})_x$  (x=3, 5) for biomedical applications have been designed and synthesized, using the cluster formula approach. The present HEAs have a single body-centered-cubic (BCC) solid-solution structure and possess prominent mechanical properties of high compressive yield strength (834–890 MPa) and microhardness (287–293 Hv), large plasticity (>45%) under compression, as well as low Young's moduli (56–68 GPa). Also, these HEAs exhibit good biocorrosion resistance, as revealed by a low corrosion rate at the order of  $10^{-4}$  mm/year and the low passive current densities of  $10^{-2}-10^{-1}$  A/m², which are attributed to the formation of passive films consisting of Ti-, Zr-, Hf-, Nb-, and Ta- oxides. The high cell viability and proliferation of bone-forming MC3T3-E1 cells on the HEAs are comparable to those on the Ti-6Al-4V alloy, indicating their good biocompatibility. The present work demonstrates the great potential of these novel Ti-Zr-Hf-Nb-Ta HEAs for biomedical applications.

### 1. Introduction

Metallic biomaterials are extensively used in medical implants, fracture-fixation devices, and orthodontic appliances due to their superior mechanical properties and good workability [1–4]. However, for the clinically commonly-used alloys (e.g., stainless steels, Co–Cr alloys, and Ti alloys), many issues are still necessary to be overcome, such as stress-shielding effects resulted from the mismatch of Young's modulus between the implants and bones, particle disease induced by corrosion and friction of the alloys, and inflammatory responses or Alzheimer's disease caused by the release toxic ions of Al and V, etc. [1–4]. The development of new biomedical alloys with the combination of low Young's moduli, superior corrosion and wear resistance, and excellent biocompatibility is necessary to meet the requirements of biomedical applications.

Recently, a new class of compositionally-complex alloys, named as

high-entropy alloys (HEAs), has garnered great attention owing to its diverse properties, including the high strength/microhardness, large ductility, and good corrosion resistance [5-15]. Among them, body-centered-cubic (BCC) HEAs have been developed, based on the early transition metals (e.g., Ti, Zr, Hf, Nb, Ta, Mo, V, and W, etc.) [11, 14–17]. Several BCC HEAs with equimolar and non-equimolar mixing in Ti-Ta-Nb-Zr [18,19], Ti-Mo-Nb-Zr [20], Ti-Mo-Ta-Nb-Zr [14, Ti-Zr-Hf-Nb-Ta [24-27], Ti-Zr-Hf-Nb [28], Ti-Nb-Hf-Ta-Zr-Mo [29] have been investigated as potential metallic biomaterials due to their high yield strength (800-1600 MPa), large plasticity and high wear resistance. In our previous study, it was found that the equimolar TiZrHfNbTa HEA consisting of biocompatible elements presents good bio-corrosion resistance and as superior biocompatibility as that of the Ti-6Al-4V alloy [30]. The Young's modulus of this TiZrHfNbTa HEA (~80 GPa) is lower than that of Ti-6Al-4V alloy (~110 GPa), but it is still much higher than those of human bones

E-mail addresses: pangshujie@buaa.edu.cn (S. Pang), zhangtao@buaa.edu.cn (T. Zhang).

<sup>\*</sup> Corresponding author. Key Laboratory of Aerospace Materials and Performance (Ministry of Education), School of Materials Science and Engineering, Beihang University, Beijing, 100191, China.

<sup>\*\*</sup> Corresponding author.

(10–30 GPa) [26]. Actually, it is still necessary to optimize and design new alloy compositions in the Ti–Zr–Hf–Nb–Ta system to further reduce the Young's modulus for biomedical applications.

A cluster formula approach has been successfully applied to design alloy compositions in multi-component complex systems [12,31-33]. It was proposed in light of chemical short-range orders (CSROs) in solid solutions, and expressed with the composition formula of [cluster](glue atoms)<sub>x</sub>, where the cluster is the nearest-neighbor polyhedron centered by a solute atom that has strong interaction (characterized by a large negative enthalpy of mixing  $\Delta H$  [32,34,35]) with the base solvent atoms to represent the strongest CSRO. The glue atoms generally have relatively-weak interactions with a number of x to match one cluster for balancing the atomic-packing density [32,34,35]. In particular, the nearest-neighbor cluster in a BCC structure is the rhombi-dodecahedron with a coordination number (CN) of 14, and the glue atom number was ideally calculated as x = 1-5 with the guide of the Friedel oscillation theory for the electron-structure stabilization [35,36]. It is emphasized that the increase in the glue atom number is dependent on whether the strong BCC-stabilized elements (V, Mo, etc.) or the weak BCC-stabilized elements (Ta, Nb, etc.) were added. In the Ti-Zr-Hf-Nb-Ta system, Ti, Zr, and Hf could be regarded as an averaged virtual element, M, since they are in the same group in the periodic table of elements, and the  $\Delta H_{\text{Ti-Zr}}$ ,  $\Delta H_{\text{Ti-Hf}}$ , and  $\Delta H_{\text{Hf-Zr}}$  are zero [37]. A similar case also occurs for Nb and Ta, which could be regarded as the element, A. Meanwhile, Zr and Hf have relatively-low elastic moduli ( $E_{\rm Zr}=68$  GPa and  $E_{\rm Hf}=78$ GPa). The high amounts of Zr and Hf may be effective on resulting in the low Young's modulus of HEAs [24,38,39]. Thus, in the present work, M serves as the cluster, and A is taken as a glum atom. The cluster formula of  $[M-M_{14}]A_x$  would be constructed owing to the weakly-positive  $\Delta H$ between M and A (such as  $\Delta H_{\text{Ti-Nb}} = + 2 \text{ kJ/mol}$  and  $\Delta H_{\text{Ti-Ta}} = + 1$ kJ/mol [37]), where  $M=Ti_{1/3}Zr_{1/3}Hf_{1/3}$  and  $A=Nb_{1/2}Ta_{1/2}$  are used since the equimolar mixing could induce a large high-entropy effect [5, 6,9,32]. Since Nb and Ta are weak BCC-stabilizers, the x = 3 and 5 are chosen to obtain the single BCC solid-solution structure [40,41]. In the present study,  $(Ti_{1/3}Zr_{1/3}Hf_{1/3})_{15}(Nb_{1/2}Ta_{1/2})_x$  (x = 3, 5) HEAs (i.e.,  $Ti_{27.78}Zr_{27.78}Hf_{27.78}Nb_{8.33}Ta_{8.33}$  and  $Ti_{25}Zr_{25}Hf_{25}Nb_{12.5}Ta_{12.5})$  with potential for biomedical applications were synthesized, and their microstructure, mechanical properties, corrosion behavior, and in vitro biocompatibility were investigated compared with those of the equi $molar Ti_{20}Zr_{20}Hf_{20}Nb_{20}Ta_{20}$  alloy.

# 2. Experimental procedures

Alloy ingots with nominal compositions of the  $Ti_{20}Zr_{20}Hf_{20}Nb_{20}Ta_{20}$ ,  $Ti_{25}Zr_{25}Hf_{25}Nb_{12.5}Ta_{12.5}$ , and  $Ti_{27.78}Zr_{27.78}Hf_{27.78}Nb_{8.33}Ta_{8.33}$  (at.%, hereafter denoted as Alloy-I, Alloy-II and Alloy-III, respectively) were fabricated by arc-melting the mixtures of the pure metals in an argon atmosphere purified using a Ti-getter. The ingots were then sealed in vacuum-quartz tubes and homogenized at 1473 K for 24 h, followed by furnace-cooling to room temperature. The phase identification was investigated by a D/max2500PC X-ray diffraction (XRD, Cu-K $\alpha$ ). The alloy microstructures were examined by a JXA8100 electron probe X-ray microanalysis (EPMA) and a JEM-2100 transmission electron microscopy (TEM). The TEM specimens were prepared by grounding the alloy slices to 50  $\mu$ m thickness and then ion-milling with a liquid-nitrogen specimen cooling stage.

Compressive mechanical properties of the Ti–Zr–Hf–Nb–Ta HEAs were carried out with a SANS CMT5504 testing machine at a strain rate of  $10^{-3}~\rm s^{-1}$ . The specimens with a dimension of  $2\times2\times4~\rm mm^3$  were machined from the ingots by an electron discharge machine, and the surfaces of these specimens were mechanically polished with the 2000-grit SiC sandpapers. After the compressive tests, the specimens were characterized by a JEOL JSM-6010LA scanning electron microscope (SEM). The Young's moduli (*E*) and indentation hardness ( $H_{\rm IT}$ ) of the alloys were determined by means of nanoindentation tests, using a nanoindenter (Keysight Technologies G200) with a standard Berkovich

tip. The surfaces of the specimens for the nanoindentation tests were mechanically ground with the 3000-grit SiC sandpapers and then polished with a Buehler MasterMet suspension on a soft cloth. Indentation was performed in the continuous stiffness mode (CSM) with a depth limit of 1  $\mu m$  using the surface approach velocity of 10 nm/s. Each specimen involved five indents to reduce test errors. The Vickers microhardness (Hv) was also measured with a Vickers microhardness tester. Densities of these alloys were calculated based on the Archimedean principle.

Corrosion behaviors of the alloys were investigated at 310 K in Hank's solution (prepared by dissolving 0.40 g/L KCl, 0.14 g/L CaCl<sub>2</sub>, 0.20 g/L MgSO<sub>4</sub>·7H<sub>2</sub>O, 0.35 g/L NaHCO<sub>3</sub>, 0.06 g/L KH<sub>2</sub>PO<sub>4</sub>, 1.00 g/L  $C_6H_{12}O_6$ , 8.00 g/L NaCl, and 0.12 g/L  $Na_2HPO_4\cdot 12H_2O$  in the distilled water) by electrochemical measurements. The specimens (10  $\times$  10  $\times$  1 mm<sup>3</sup>) were ground with 2000-grit SiC sandpapers, followed by washing in the acetone, ethanol, and distilled water. The Ti-6Al-4V alloy (denoted as Ti64) was also examined as the reference material. The electrochemical properties were examined by a Princeton VersaSTAT III electrochemical workstation with a standard three-electrode cell system. A sample was employed as the working electrode. A saturated calomel electrode (SCE) was chosen as the reference electrode. The platinum foil was used as a counter electrode. The corrosion specimen was immersed in the solution for 1800 s to get a steady state of the open-circuit potential (OCP), and then the potentiodynamic-polarization tests were performed with a sweeping range of 50 mV below the OCP to 2 V at a sweeping rate of 0.833 V/s. The surface compositions of the specimens exposed to air were studied by a ThermoFisher Scientific ESCALAB 250 X-ray photoelectron spectroscopy (XPS, monochromatic Al-Kα).

Mouse MC3T3-E1 cells were used to estimate the in vitro biocompatibility of the HEAs. The specimens ( $\phi$  6 mm  $\times$  1 mm) were ground with 3000-grit SiC sandpapers and then washed in the ethanol and distilled water. Prior to the cell-culture experiments, all the specimens were sterilized by the exposure to an ultraviolet (UV) light for at least 3 h. The cell-culture experiments were performed according to the procedures described in Ref. [42]. The viability of cells was evaluated with a fluorescent dye (LIVE/DEAD Viability/Cytotoxicity Kit). After 72-h incubation, the cells were rinsed with the phosphate-buffered saline (PBS) and then stained with the PBS containing 2  $\mu M$  calcein and 4  $\mu M$ propidium iodide (PI) in the dark for 15 min at room temperature. After that, the viable (green) and dead (red) cells were observed under a laser scanning confocal microscope (Olympus FV1200). After incubation for 1, 3, and 5 days, the MTT assay [MTT: 3-(4,5-dimethylthiazol-2-yl)-2, 5-diphenyl tetrazolium bromide] was utilized to exam the cell-proliferation behaviors. The procedures were the same as those in Ref. [43]. The absorbance was carried out at 570 nm using a microplate reader. At least triplicate specimens were used in all cell-culture experiments for reproducibility. The statistical significance of differences was assessed employing the Student's t-test.

## 3. Results

# 3.1. Microstructure

The XRD patterns of the homogenized Ti–Zr–Hf–Nb–Ta alloys are shown in Fig. 1(a). Only one group of diffraction peaks corresponding to the BCC phase is observed in the pattern of each alloy, indicating that the Alloy-I, Alloy-II, and Alloy-III alloys consist of the single BCC solid solutions without any intermetallic compounds. As displayed in Fig. 1 (b), with decreasing the Nb and Ta contents, the enlarged (110) peaks at  $36^{\circ}$ –38° tend to shift to the lower 20 angle, suggesting the increase in the lattice parameters of HEAs (Table 1). This phenomenon is attributed to the solid-solution-induced expansion by the higher contents of Zr and Hf with a relatively-large atomic radius (r<sub>Zr</sub> = 155.1 p.m. and r<sub>Hf</sub> = 151.4 p. m.). To further investigate the microstructures, the typical SEM backscattered-electron (BSE) images of the homogenized Alloy-II and Alloy-III and the corresponding elemental mapping obtained by means

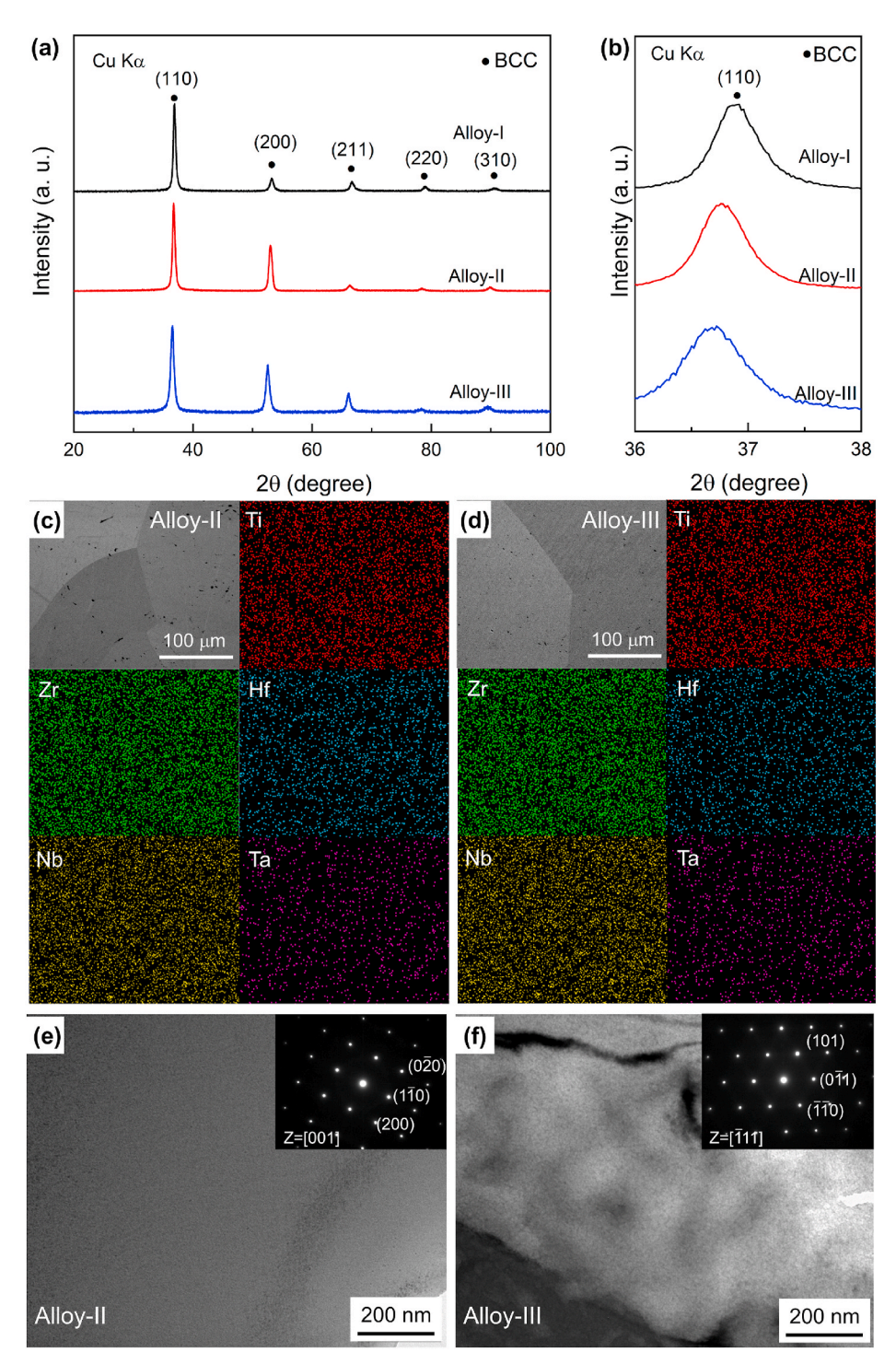


Fig. 1. (a) XRD patterns and (b) the enlarged (110) diffraction peaks of the equiatomic TiZrHfNbTa (Alloy-I) and the  $(Ti_{1/3}Zr_{1/3}Hf_{1/3})_{15}(Nb_{1/2}Ta_{1/2})_x$  (x = 3, 5) (Alloy-II and Alloy-III, respectively); (c–d) SEM-BSE with the corresponding EPMA elemental mapping results and (e–f) TEM images with the inset showing the SAED patterns of Alloy-III and Alloy-III.

Table 1
Lattice parameter (a), density (ρ), yield strength (σ<sub>0,2</sub>), plastic strain (ε), Vickers microhardness (Hv), Young's modulus (E), Hv/E, Mo<sub>eq</sub> values, and valence electron concentration (VEC) of the Alloy-II, Alloy-II, and Alloy-III.

Alloy	a (Å)	$\rho$ (g cm <sup>-3</sup> )	σ <sub>0.2</sub> (MPa)	ε (%)	Hv	E (GPa)	Hv/E	Mo <sub>eq</sub> (wt.%)	VEC
Alloy-I	3.432	$9.72\pm0.02$	926	>50	$320\pm 5$	$79\pm3$	0.043	21.1	4.4
Alloy-II	3.448	$9.22\pm0.01$	890	>50	$293\pm7$	$68 \pm 4$	0.047	16.3	4.25
Alloy-III	3.465	$8.83\pm0.01$	834	~45	$287\pm4$	$56 \pm 2$	0.051	13.5	4.17

of EPMA are shown in Fig. 1(c) and (d). It is seen that after homogenization, all these alloys consist of equiaxed grains, and the decrease in the amounts of Nb and Ta does not lead to the elemental segregation or second-phase precipitation. The bright-field TEM (BF-TEM) images and the corresponding selected area electron diffraction (SAED) patterns of Alloy-II and Alloy-III are displayed in Fig. 1(e) and (f). There are no precipitated phases in the alloys, as shown in the BF-TEM images. In the SAED patterns (the inset), only the diffraction spots of a BCC phase can be recognized, further confirming the formation of the single BCC solid solution with no other phases in the novel HEAs.

# 3.2. Mechanical properties

The compressive true stress-strain curves of the Ti-Zr-Hf-Nb-Ta HEAs are displayed in Fig. 2(a), from which the values of the yield strengths ( $\sigma_{0,2}$ ) taken at a plastic strain of 0.2% and plastic strain ( $\varepsilon$ ) are extracted and listed in Table 1. The HEAs exhibit linear-elastic deformation, followed by yielding at 834-926 MPa, and then the stresses continuously increase up to 878-1068 MPa with the increment in the strain due to the work hardening. Afterwards, the true stresses decrease upon the following loading due to the increase in the diameters of the specimens. The Alloy-I and Alloy-II were unfractured after the compressive deformation with  $\varepsilon > 50\%$ , and the plastic strain of the Alloy-III is about 45%. The morphologies of these HEAs after the compressive tests were further observed by SEM. As shown in Fig. 2(b) and (c), the surfaces of the Alloy-I and Alloy-II exhibit obvious buckling without visible microcracks. For the Alloy-III alloy with lower Nb and Ta contents, some micro- and macro-cracks are observed on the surfaces of the fractured sample along the direction of the main shear stress, as shown in Fig. 2(d). The initiation and propagation of cracks during compression lead to the fracture of the alloys. In addition, the alloys possess high Vickers microhardness (Hv) of about 287-320, as listed in Table 1. The Hv and density  $(\rho)$  values of these HEAs reduce with decreasing the Nb and Ta contents.

The Young's modulus (E) and indentation hardness ( $H_{\rm IT}$ ) of the HEAs were tested by nanoindentation. Fig. 3 displays the representative load

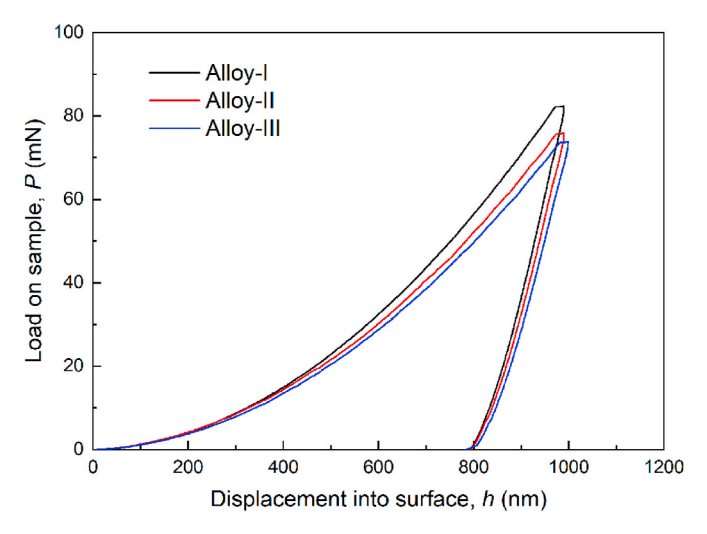


**Fig. 3.** *P-h* curves under nanoindentation for Alloy-I, Alloy-II, and Alloy-III tested with a Berkovich indenter.

(*P*)-displacement (*h*) nanoindentation curves. The *E* and  $H_{\rm IT}$  values are calculated from Fig. 3, using the Oliver-Pharr method, as used in Ref. [44]. For comparison, the obtained  $H_{\rm IT}$  values can be converted into the equivalent Vickers hardness, *H*IT v values with a relation of *H*IT v = 0.9081  $H_{\rm IT}$  for a Berkovich indentation tip [45]. These HEAs possess high hardness, *H*IT v in the range of 3.53–3.97 GPa. The *H*IT v value is about 25% higher than the *H*v value due to the indenter-size effect [44, 46]. The Young's modulus of Alloy-I is about 79 GPa, which is consistent with the reported value [26]. With the decrease in the Ta and Nb contents, the Alloy-II and Alloy-III exhibit reduced Young's modulus of ~68 GPa and ~56 GPa, respectively. The integration of low Young's moduli, high strength, good plasticity, and high hardness of the novel HEAs are favorable for the biomedical applications.

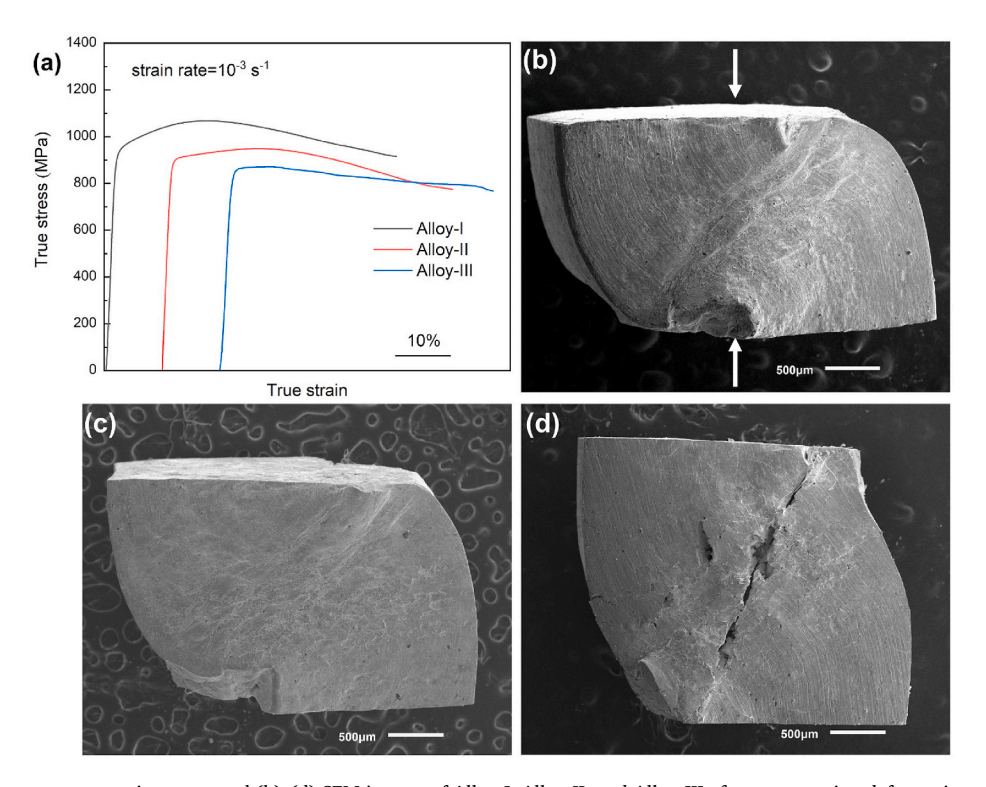
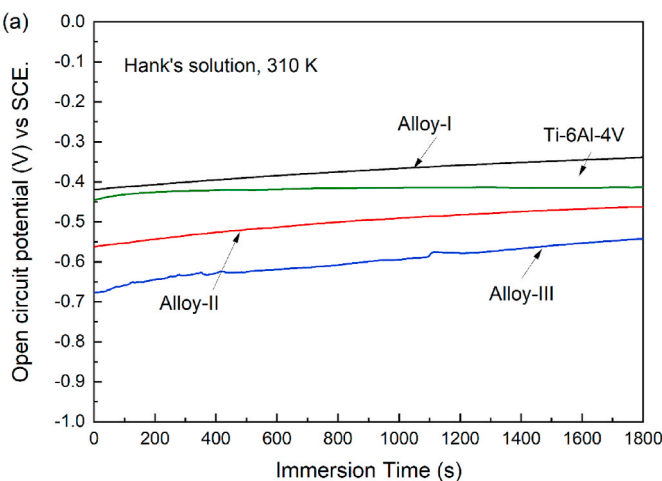


Fig. 2. (a) Compressive true stress—strain curves and (b)—(d) SEM images of Alloy-I, Alloy-II, and Alloy-III after compression deformation, respectively. (The white arrows indicate the compressive loading direction.).

#### 3.3. Bio-corrosion behaviors

To characterize the bio-corrosion behavior of the Ti-Zr-Hf-Nb-Ta alloys, electrochemical measurements on these alloys and the Ti64 were conducted at 310 K in Hank's solution for simulating the body fluid environment. The changes in the OCPs with immersion time of the alloys are displayed in Fig. 4(a). The OCPs of these alloys shift toward positive potential direction initially and then slow down to achieve steady values, implying an improved stability of the surface films during the immersion. After immersion for 1800 s, compared with the Ti64, the non-equiatomic HEAs possess lower OCPs in the range of - 0.55 - - 0.45 V, and the equiatomic TiZrHfNbTa HEA has higher OCP of about - 0.35 V. It implies that the stability of the surface films on the alloys exhibits a deteriorating tendency with the decrease in the amounts of Nb and Ta. The potentiodynamic-polarization plots of the HEAs and the Ti64 are displayed in Fig. 4(b). All the alloys are spontaneously passivated with passive current densities ( $i_{pass}$ ) around  $10^{-2} - 10^{-1}$  A/m<sup>2</sup>, although the Alloy-III suffers pitting corrosion, as revealed by the abrupt rise in the current density at the high potential of ~1.238 V. The corrosion parameters derived from the polarization curves are summarized in Table 2. With the decrement in the Nb and Ta contents of the alloys, the corrosion potentials ( $E_{corr}$ ) exhibit a decreasing tendency, whereas the corrosion current densities ( $i_{corr}$ ) are on the same order of  $10^{-3}$  A/m<sup>2</sup> and show no distinguishable difference. Moreover, as presented in Table 2, the corrosion rates calculated from the  $i_{corr}$  of the Ti-Zr-Hf-Nb-Ta HEAs are at the order of 10<sup>-4</sup> mm/year. These results



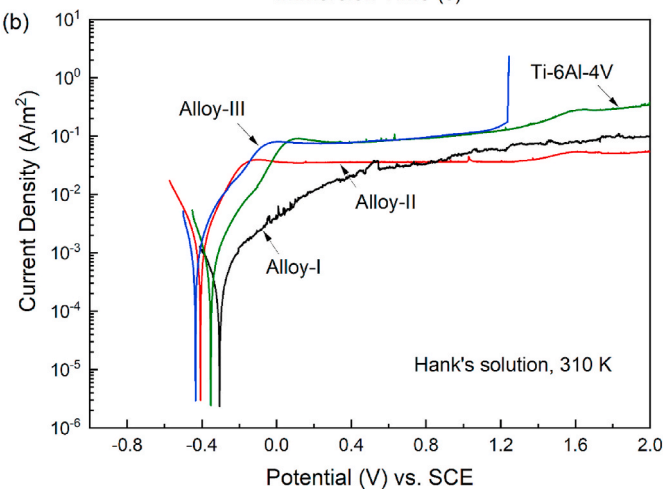


Fig. 4. (a) Changes in the open circuit potential with immersion time and (b) potentiodynamic-polarization curves of Alloy-II, Alloy-III, and Ti-6Al-4V in Hank's solution at 310 K.

**Table 2**Values of corrosion parameters derived from the potentiodynamic-polarization curves of the Alloy-I, Alloy-II, Alloy-III, and Ti64 in Hank's solution at 310 K.

Alloy	$E_{corr}$ (V)	$i_{corr}$ ( $ imes 10^{-3}$ A/m <sup>2</sup> )	$E_{pit}$ (V)	Corrosion rate ( $\times$ $10^{-4}$ mm/y)
Alloy-I	$-0.302 \pm 0.014$	$0.08 \pm 0.20$	-	$5.5\pm1.5$
Alloy- II	$-0.407 \pm 0.021$	$1.19 \pm 0.42$	-	$8.8\pm2.8$
Alloy- III	$-0.437 \pm 0.062$	$1.22\pm0.37$	$1.238 \pm 0.019$	$9.3\pm3.1$
Ti64	$-0.347 \pm \\ 0.014$	$0.61\pm0.14$	-	$5.1\pm1.2$

indicate the good bio-corrosion resistance of these HEAs in the aggressive physiological fluid.

For a further understanding of the corrosion behavior of the Ti-Zr-Hf-Nb-Ta HEAs, the chemical composition of the passive films on these HEAs exposed to air was evaluated by the XPS. The XPS spectra exhibited peaks of carbon, oxygen, niobium, titanium, zirconium, hafnium and tantalum. The C 1s peaks are related to the surface carbon contamination of the specimens. The high-resolution spectra are demonstrated in Fig. 5. The spectra of O 1s show three peaks corresponding to O<sup>2-</sup>, OH<sup>-</sup>, and absorbed H<sub>2</sub>O. The spectra of Ti 2p and Zr 3d consist of peaks corresponding to Ti  $^{4+}$  (2p $_{3/2}$  and 2p $_{1/2}$ ) and Zr $^{4+}$  (3d $_{3/2}$ and 3d<sub>5/2</sub>), respectively, implying that these two elements in the surface films are in the dioxide state. The metallic Ti and Zr in the underlying alloy surfaces can be also detected in the spectra of Ti 2p and Zr 3d, respectively. The spectra of Hf 4f are composed of the peaks associated with HfO<sub>2</sub> and Hf<sup>0</sup>. The de-convoluted Nb 3d spectra show the peaks corresponding to Nb<sub>2</sub>O<sub>5</sub> (Nb<sup>5+</sup>) and Nb<sup>0</sup>. A peak of Hf 4d<sub>5/2</sub> is also detected in Fig. 5(e), which is overlapped with the Nb 3d region. In Fig. 5 (f), the presence of Ta in both metallic (Ta<sup>0</sup>) and oxidized states (Ta<sub>2</sub>O<sub>5</sub>) are seen on the Ta 4f spectra. The cationic concentrations in the airformed surface films of the HEAs are quantified in Fig. 6, where ox represents oxidized states. It is seen that the surface films formed on the HEAs consist of higher contents of Zr and Hf cations and lower contents of Ti and Ta, in comparison with the nominal compositions. The fractions of Nb cations in the surface film of each alloy are similar to those in alloys. This result indicates the preferential oxidation of Zr and Hf for the alloys. Therefore, the air-formed surface films on the HEAs mainly consist of the chemically-stable oxides, which could be responsible for the good corrosion resistance of the HEAs.

# 3.4. In vitro biocompatibility

The biocompatibility of these Ti-Zr-Hf-Nb-Ta HEAs was evaluated by the direct cell-culture experiment, employing the MC3T3-E1 cells. The viability of cells on the HEAs and Ti64 after culturing for 72 h was observed by fluorescent staining. As displayed in Fig. 7, numerous MC3T3-E1 cells are found attached onto the surfaces of the HEAs and Ti64, and the adherent cells are highly viable, suggesting high viability and good initial adhesion of the MC3T3-E1 cells on the HEAs. Furthermore, the quantities of the adhered cells on the different HEAs are presented as the percentages of the result on the Ti64 and shown in Fig. 8. No distinguished statistical-difference in the cell numbers is observed on the various substrates, implying the good cell viability on the HEAs, comparable to that on the Ti64. As presented in Fig. 9, the cell-proliferation behaviors on the HEAs and Ti64 are evaluated, using the MTT assay after the 1-, 3- and 5-day incubation. The absorbance, corresponding to the viable cell numbers, gradually increases from days 1-5, indicating the continuous proliferation of the cells. At day 1, the absorbance of the HEAs is slightly lower than that of the Ti64, while at days 3 and 5, the absorbance of the HEAs is slightly better than that of the Ti64. At each time point, no statistical difference in the cell proliferation on the HEAs and Ti64 is found, indicating the good cell

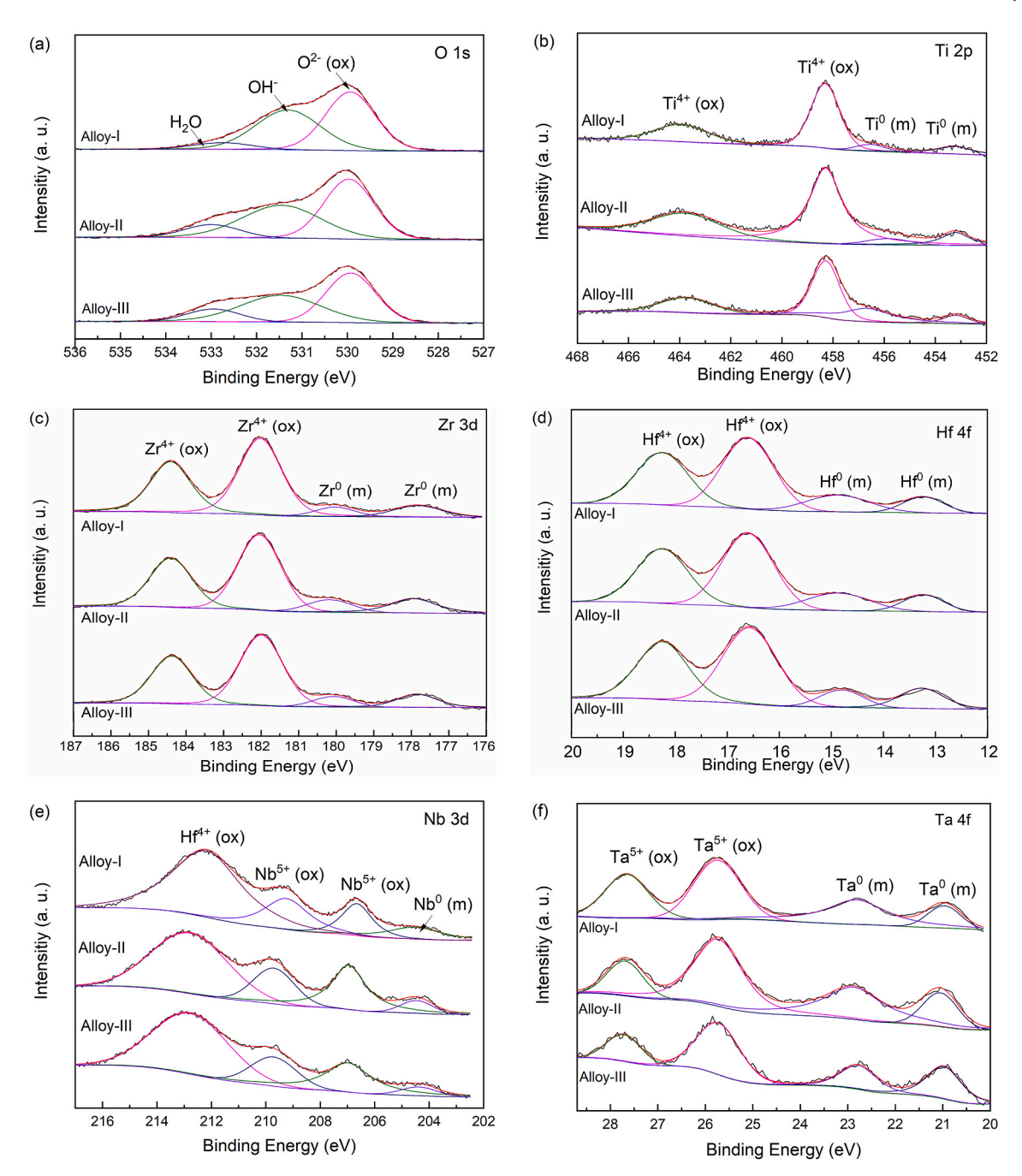


Fig. 5. XPS spectra of (a) O 1s, (b) Ti 2p, (c) Zr 3d, (d) Hf 4f, (e) Nb 3d, and (f) Ta 4f for the surface films on the Alloy-I, Alloy-II, and Alloy-III exposed to air.

proliferation on the HEAs parallel to that on the Ti64.

### 4. Discussion

In the past decade, a number of BCC HEAs have attracted interests as potential biomaterials, especially for the dental and orthopedic implants, owing to their high yield strength (900–1600 MPa), excellent biocompatibility, and good corrosion and wear resistance [14,18–24,30, 33,39,47]. In this work, the Ti–Zr–Hf–Nb–Ta HEAs composed of biocompatible elements with low Young's moduli are designed by a cluster formula approach. The newly-developed HEAs exhibit an integration of low Young's moduli (56–68 GPa), high yield strength (834–890 MPa), and good anti-corrosion performance and *in vitro* biocompatibility, which are favorable for biomedical applications.

As demonstrated in the result, the  $(Ti_{1/3}Zr_{1/3}Hf_{1/3})_{15}(Nb_{1/2}Ta_{1/2})_x$ 

 $(x=3,\,5)$  HEAs have a single BCC solid-solution structure. The molybdenum equivalent ( $Mo_{eq}$ ) has been widely used to quantitatively measure the  $\beta$ -phase stability in the multicomponent Ti-based alloys [40, 48]. It has been proposed that the  $Mo_{eq}$  parameter is also effective for predicting the phase stability of BCC/HCP solid solutions in the HEAs [29]. The  $Mo_{eq}$  values of the present HEAs can be calculated and listed in Table 1 using Eq. (1) [49]:

$$Mo_{eq} = 1.00[Mo] + 0.64[Nb] + 0.23[Ta] + 0.05[Hf] + 0.16[Zr] + 0.71[Pd] + 0.97[Si] + 0.80[V] + 0.56[W]$$
(1)

where [M] is the concentration of M element in weight percent. For a specific alloy system, the larger the  $Mo_{eq}$  values are, the better the  $\beta$  phase stability for the Ti alloy is [29,40,48]. According to Eq. (1), in the Ti–Zr–Hf–Nb–Ta HEAs system, the values of  $Mo_{eq}$  are in the range of 13.5–21.1 wt.% and larger than 12 wt.%, indicating a high tendency for

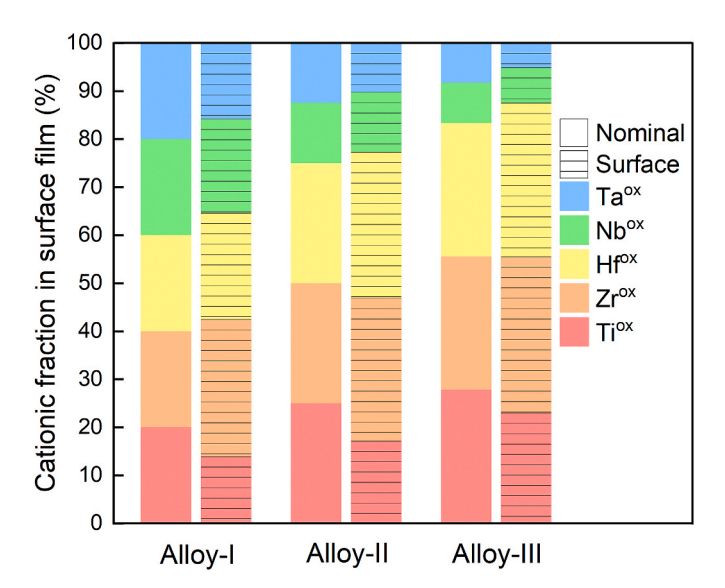


**Fig. 6.** Cationic fractions of surface films on Alloy-I, Alloy-II, and Alloy-III exposed to air. The nominal contents of the alloy constituents are also shown for comparison.

the formation of a BCC phase [29]. Additionally, the valence electron concentration (VEC) has been used to predict the phase stability of HEAs [50]. The VEC of the HEAs are found to be lower than 6.87. Thus, the present Ti–Zr–Hf–Nb–Ta HEAs are expected to form a single BCC phase [50], which is actually consistent with the experimental results. Meanwhile, the decrease in the values of VEC may result in decreasing the Young's moduli of these HEAs [24].

The novel HEAs exhibit high yield strengths of 834–890 MPa, which could be ascribed to solid-solution strengthening caused by synergetic misfits among atoms [6–8,15]. More importantly, the Young's moduli of the present Ti–Zr–Hf–Nb–Ta HEAs ranged from  $\sim$ 56 to 68 GPa, which are much lower than that of Ti64 ( $\sim$ 110 GPa) [3,4]. As is well known, the Young's moduli of the alloys are closely related to crystalline structures. The BCC structure generally possesses a lower Young's modulus, compared with the HCP structure [51]. The studied HEAs exhibit the single BCC structures. It is known that the Young's modulus

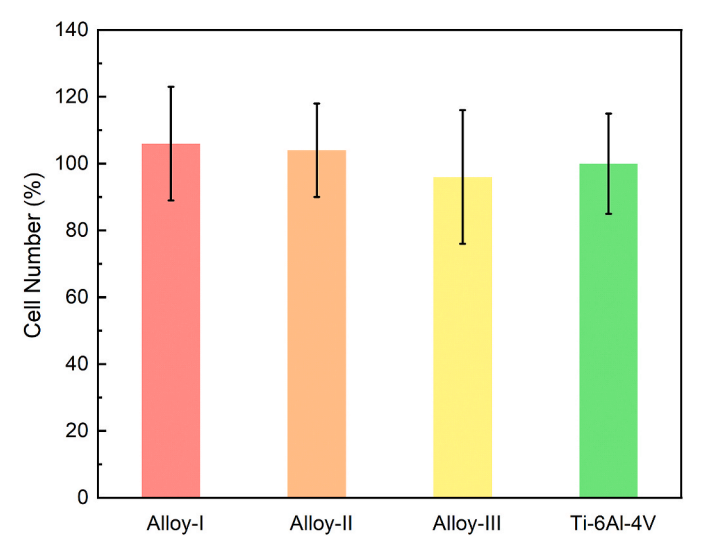


**Fig. 8.** Cell numbers attached to Alloy-I, Alloy-II, Alloy-II, and Ti64 (presented as percentages of cells attached to the Ti64) after cell culture for 72 h.

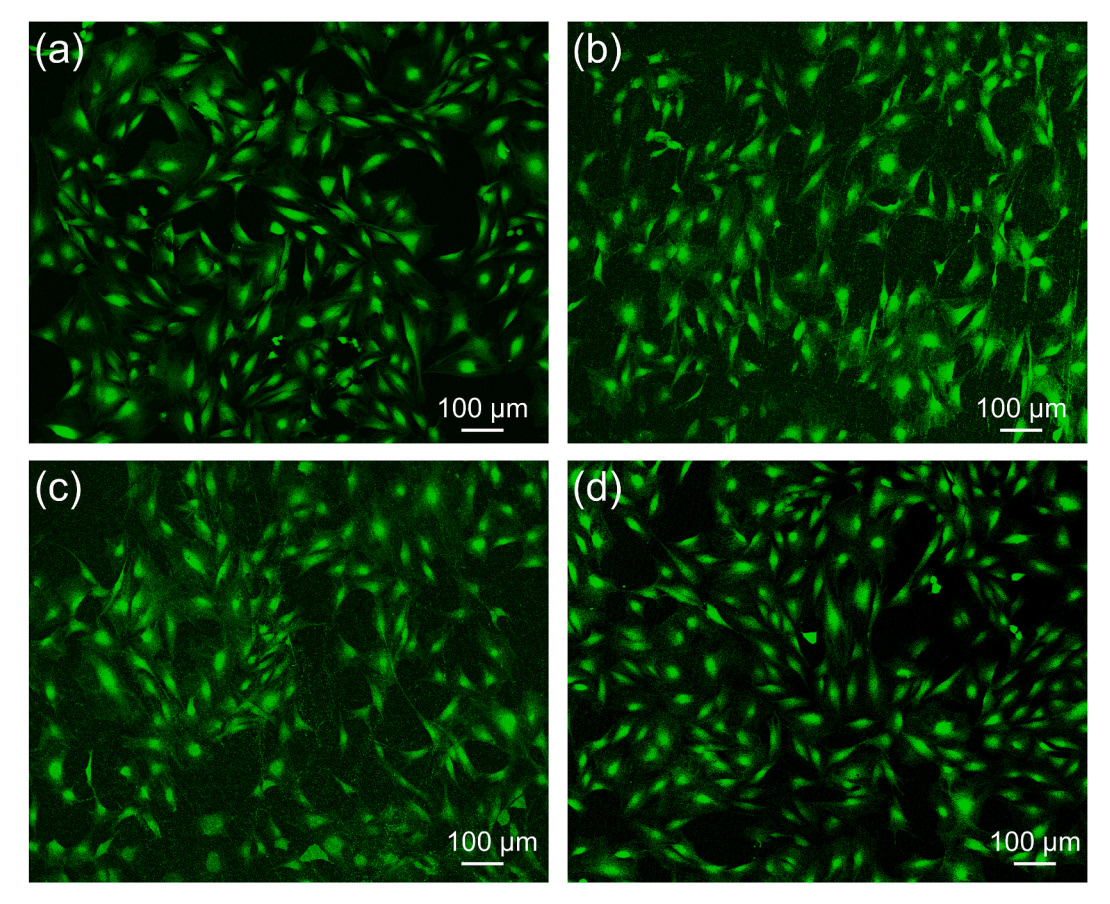


Fig. 7. Live/dead staining of MC3T3-E1 cells on (a) Alloy-I, (b) Alloy-II, (c) Alloy-III, and (d) Ti64 after 72 h incubation.

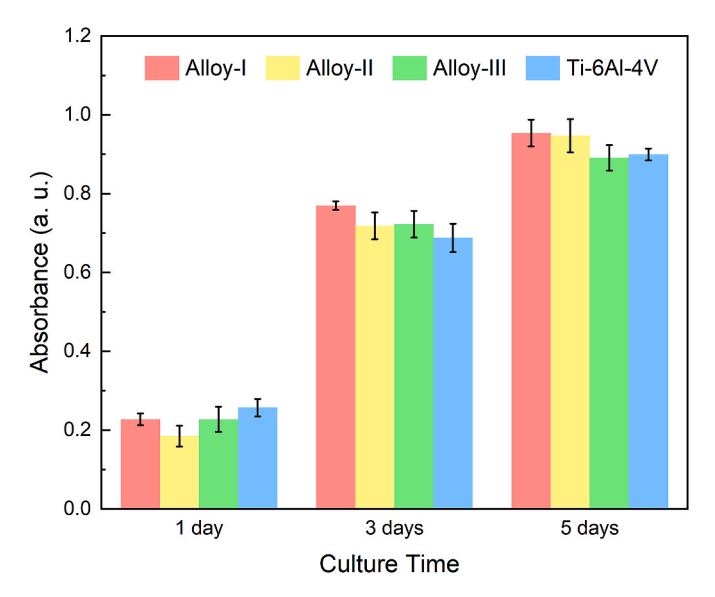


Fig. 9. Proliferation of MC3T3-E1 cells on Alloy-I, Alloy-II, Alloy-III, and Ti64 after cell culture for 1, 3 and 5 days, respectively.

of a BCC polycrystalline alloy is closely related to its single-crystal elastic constants (SECs), i.e.,  $C_{11}$ ,  $C_{12}$ , and  $C_{44}$  [51]. It is evident that in the BCC-structure Zr- and Ti-based alloys, the lower Young's modulus can be achieved by making smaller  $C_{11}$ ,  $C_{12}$ , and  $C_{44}$  [52,53]. Furthermore, the SECs of BCC metals are generally reduced with the decrease of d + selectrons (i.e., the valence electrons for transitional metals) [54]. Therefore, the present single BCC HEAs possess low Young's moduli due to their low VECs to obtain small C<sub>11</sub>-C<sub>12</sub> values and retaining the BCC structure simultaneously. Meanwhile, the high amounts of Zr and Hf with relatively-low elastic moduli ( $E_{Zr} = 68$  GPa, and  $E_{Hf} = 78$  GPa) are contributed to the low Young's moduli of HEAs. Additionally, the present HEAs exhibit the microhardness (287-293 Hv), while the Hv/E values of the HEAs are about  $\sim$ 0.043–0.047, which are higher than that of the Ti64 ( $\sim$ 0.026) [27]. It has been reported that a higher ratio of the hardness to Young's modulus (Hv/E) generally corresponds to a better wear resistance [55]. The high hardness and Hv/E values imply that the HEAs would possess good wear resistance, preventing wear debris and reducing the risk of particle disease. Thus, the combination of low Young's moduli, high yield strength and Hv/E values indicates that the Ti-Zr-Hf-Nb-Ta HEAs have good mechanical compatibility for biomedical applications.

Good anti-corrosion performance of the biomedical materials in the corrosive physiological fluids is a key aspect for orthopedic implants to inhibit the release of metallic ions into the tissue and guarantee the implant integrity during long-term service. Revealed by the electrochemical measurements, the present HEAs exhibit good anti-corrosion properties comparable to the Ti64. The good anti-corrosion performance of the HEAs is attributed to the alloy compositions, constituent phases, and the formation of the passive films on the HEAs. It is well known that the present HEAs are composed of valve metals and passivated elements, which can promote the protectiveness of passive films of the alloys [30,47,56]. The surface films of the HEAs consist of chemically-stable Ta<sub>2</sub>O<sub>5</sub>, Nb<sub>2</sub>O<sub>5</sub>, TiO<sub>2</sub>, HfO<sub>2</sub>, and ZrO<sub>2</sub>, which are favorable to form passive films with high protectiveness [14,21,27,30, 47,57]. Moreover, the studied HEAs have the single BCC solid-solution structure, and the elements are uniformly distributed, which is beneficial for the formation of homogeneous protective passive films on the alloy surfaces. Therefore, the good anti-corrosion properties of these HEAs could be attributed to the formation of the homogeneous protective passive film consisting of the chemically-stable oxides on the HEAs. Moreover, the Alloy-I exhibit better corrosion resistance than the Alloy-II and Alloy-III. It is known that usually the oxides of Nb and Ta

 $(\mathrm{Nb_2O_5}$  and  $\mathrm{Ta_2O_5})$  are more protective than the oxides of other constituent elements in these alloys, and the enrichment of Nb and Ta in the surface films may lead to the better corrosion resistance [14,27,30,56,57]. In comparison with the non-equimolar TiZrHfNbTa HEAs and the Ti64, the higher contents of Nb and Ta of the equimolar TiZrHfNbTa HEA should result in the higher contents of Nb and Ta in the surface film, which was also confirmed by the results of the XPS analysis (Figs. 5 and 6). For the Alloy-III, pitting corrosion occurred at a high potential, which could be attributed to the susceptibility of HfO<sub>2</sub> and ZrO<sub>2</sub> to the chloride ions in the Hank's solution [30,42].

The *in vitro* biocompatibility of the Ti–Zr–Hf–Nb–Ta HEAs investigated using the MC3T3-E1 pre-osteoblasts indicated that the HEAs can support initial cell adhesion with high cell viability similar to the Ti64. Additionally, the successful proliferation behavior guarantees that the alloys would not induce adverse effects on the cell incubation. No significant difference is found in the cell responses to these HEAs, demonstrating little influence of the alloy compositions on the biocompatibility. The good biocompatibility of the present HEAs is mainly due to the formation of the non-cytotoxic surface film consisting of biocompatible elements [3,23,38,42,58,59]. Furthermore, the high corrosion resistance would ensure the good biocompatibility by effectively preventing releasing metal ions during implantation [14,23,30, 42,43,47]. Thus, the novel  $(Ti_{1/3}Zr_{1/3}Hf_{1/3})_{15}(Nb_{1/2}Ta_{1/2})_x$  (x=3, 5) HEAs with the good biocompatibility are promising biomedical materials.

#### 5. Conclusions

In this study,  $(Ti_{1/3}Zr_{1/3}Hf_{1/3})_{15}(Nb_{1/2}Ta_{1/2})_x$  (x = 3, 5) HEAs with single BCC structures have been designed, using the cluster formula approach. The microstructure, mechanical properties, and bio-corrosion behavior of the HEAs were investigated. The homogenized HEAs consist of single BCC structures with equiaxed grains. The HEAs possess high compressive yield strength in the range of about 834-890 MPa, and good plasticity (>45%) under compression. The HEAs also exhibit low Young's moduli of about 56-68 GPa, which are lower than that of the Ti-6Al-4V alloy. Good bio-corrosion resistance of the Ti-Zr-Hf-Nb-Ta HEAs has been characterized by the low passive current densities of  $10^{-2}$  $-10^{-1}$  A/m<sup>2</sup>, low corrosion rates at the order of  $10^{-4}$  mm/year, and no occurrence of pitting under the anodic polarization up to 1.238 V at 310 K in Hank's solution. The good bio-corrosion resistance of the HEAs is ascribed to the formation of the passive films consisting of HfO<sub>2</sub> ZrO<sub>2</sub>, TiO<sub>2</sub>, Ta<sub>2</sub>O<sub>5</sub>, and Nb<sub>2</sub>O<sub>5</sub> on the alloy surface. The HEAs can support the initial cell adherent and proliferation with high viability, demonstrating the good biocompatibility of the HEAs. The novel Ti-Zr-Hf-Nb-Ta HEAs are promising candidates for biomaterials due to their prominent mechanical properties, especially, the relatively-low Young's moduli, good bio-corrosion resistance and biocompatibility.

# CRediT authorship contribution statement

Wei Yang: Methodology, Investigation, Data Curation, Writing - original draft. Shujie Pang: Conceptualization, Supervision, Writing - review & editing, Resources, Funding acquisition. Ying Liu: Methodology, Writing - review & editing. Qing Wang: Conceptualization, Writing - review & editing. Peter K. Liaw: Writing - review & editing. Tao Zhang: Resources, Supervision.

# Declaration of competing interest

The authors declare that they have no known competing financial interests or personal relationships that could have appeared to influence the work reported in this paper.

#### Acknowledgements

This work was financially supported by the National Natural Science Foundation of China (Grant Nos. 51971007 and 51701008) and the 111 Project (B17002). P. K. L. very much acknowledges the support from the National Science Foundation [DMR-1611180 and 1809640].

#### References

- [1] Q. Chen, G.A. Thouas, Metallic implant biomaterials, Mater. Sci. Eng. R 87 (2015) 1–57
- [2] M. Long, H.J. Rack, Titanium alloys in total joint replacement—a materials science perspective, Biomaterials 19 (1998) 1621–1639.
- [3] M. Niinomi, Recent metallic materials for biomedical applications, Metall. Mater. Trans. 33 (2002) 477–486.
- [4] S.V. Muley, A.N. Vidvans, G.P. Chaudhari, S. Udainiya, An assessment of ultra fine grained 316L stainless steel for implant applications, Acta Biomater. 30 (2016) 408, 419
- [5] J.W. Yeh, S.K. Chen, S.J. Lin, J.Y. Gan, T.S. Chin, T.T. Shun, C.H. Tsau, S.Y. Chang, Nanostructured high-entropy alloys with multiple principal elements: novel alloy design concepts and outcomes, Adv. Eng. Mater. 6 (2004) 299–303.
- [6] Y. Zhang, T.T. Zuo, Z. Tang, M.C. Gao, K.A. Dahmen, P.K. Liaw, Z.P. Lu, Microstructures and properties of high-entropy alloys, Prog. Mater. Sci. 61 (2014) 1, 03
- [7] D.B. Miracle, O.N. Senkov, A critical review of high entropy alloys and related concepts, Acta Mater. 122 (2017) 448–511.
- [8] W. Li, D. Xie, D. Li, Y. Zhang, Y. Gao, P.K. Liaw, Mechanical behavior of high-entropy alloys, Prog. Mater. Sci. 118 (2021) 100777.
- [9] E.P. George, D. Raabe, R.O. Ritchie, High-entropy alloys, Nat. Rev. Mater. 4 (2019)
- [10] B. Cantor, I.T.H. Chang, P. Knight, A.J.B. Vincent, Microstructural development in equiatomic multicomponent alloys, Mater. Sci. Eng. A 375–377 (2004) 213–218.
- [11] Z.F. Lei, X.J. Liu, Y. Wu, H. Wang, S.H. Jiang, S.D. Wang, X.D. Hui, Y.D. Wu, B. Gault, P. Kontis, D. Raabe, L. Gu, Q.H. Zhang, H.W. Chen, H.T. Wang, J.B. Liu, K. An, Q.S. Zeng, T.G. Nieh, Z.P. Lu, Enhanced strength and ductility in a highentropy alloy via ordered oxygen complexes, Nature 563 (2018) 546–550.
- [12] Y. Ma, Q. Wang, X. Zhou, J. Hao, B. Gault, Q. Zhang, C. Dong, T.G. Nieh, A novel soft-magnetic B2-based multiprincipal-element alloy with a uniform distribution of coherent body-centered-cubic nanoprecipitates, Adv. Mater. 33 (2021) 2006723.
- [13] X.L. Yan, H. Guo, W. Yang, S.J. Pang, Q. Wang, Y. Liu, P.K. Liaw, T. Zhang, Al<sub>0.3</sub>Cr<sub>x</sub>FeCoNi high-entropy alloys with high corrosion resistance and good mechanical properties, J. Alloys Compd. 860 (2021) 158436.
- [14] N.B. Hua, W.J. Wang, Q.T. Wang, Y.X. Ye, S.H. Lin, L. Zhang, Q.H. Guo, J. Brechtl, P.K. Liaw, Mechanical, corrosion, and wear properties of biomedical Ti–Zr–Nb–Ta–Mo high entropy alloys, J. Alloys Compd. 861 (2021) 157997.
- [15] J.P. Couzinié, G. Dirras, Body-centered cubic high-entropy alloys: from processing to underlying deformation mechanisms, Mater. Char. 147 (2019) 533–544.
- [16] O.N. Senkov, G.B. Wilks, D.B. Miracle, C.P. Chuang, P.K. Liaw, Refractory highentropy alloys. Intermetallics 18 (2010) 1758–1765.
- [17] F.X. Zhang, Y. Tong, M. Kirkham, A. Huq, H. Bei, W.J. Weber, Y. Zhang, Structural disorder, phase stability and compressibility of refractory body-centered cubic solid-solution alloys, J. Alloys Compd. 847 (2020) 155970.
- [18] V.T. Nguyen, M. Qian, Z. Shi, T. Song, L. Huang, J. Zou, A novel quaternary equiatomic Ti-Zr-Nb-Ta medium entropy alloy (MEA), Intermetallics 101 (2018) 39-43.
- [19] V.T. Nguyen, M. Qian, Z. Shi, T. Song, L. Huang, J. Zou, Compositional design of strong and ductile (tensile) Ti-Zr-Nb-Ta medium entropy alloys (MEAs) using the atomic mismatch approach, Mater. Sci. Eng. A 742 (2019) 762–772.
- [20] K. Wong, H. Hsu, S. Wu, W. Ho, Structure and properties of Ti-rich Ti-Zr-Nb-Mo medium-entropy alloys, J. Alloys Compd. 868 (2021) 159137.
- [21] S. Wang, J. Xu, TiZrNbTaMo high-entropy alloy designed for orthopedic implants: as-cast microstructure and mechanical properties, Mater. Sci. Eng. C 73 (2017) 80–89
- [22] T. Hori, T. Nagase, M. Todai, A. Matsugaki, T. Nakano, Development of non-equiatomic Ti-Nb-Ta-Zr-Mo high-entropy alloys for metallic biomaterials, Scripta Mater. 172 (2019) 83–87.
- [23] M. Todai, T. Nagase, T. Hori, A. Matsugaki, A. Sekita, T. Nakano, Novel TiNbTaZrMo high-entropy alloys for metallic biomaterials, Scripta Mater. 129 (2017) 65–68.
- [24] Y. Yuan, Y. Wu, Z. Yang, X. Liang, Z. Lei, H. Huang, H. Wang, X. Liu, K. An, W. Wu, Z. Lu, Formation, structure and properties of biocompatible TiZrHfNbTa highentropy alloys, Mater. Res. Lett. 7 (2019) 225–231.
- [25] O.N. Senkov, J.M. Scott, S.V. Senkova, D.B. Miracle, C.F. Woodward, Microstructure and room temperature properties of a high-entropy TaNbHfZrTi alloy, J. Alloys Compd. 509 (2011) 6043–6048.
- [26] G. Dirras, L. Lilensten, P. Djemia, M. Laurent-Brocq, D. Tingaud, J.P. Couzinié, L. Perrière, T. Chauveau, I. Guillot, Elastic and plastic properties of as-cast equimolar TiHfZrTaNb high-entropy alloy, Mater. Sci. Eng. A 654 (2016) 30–38.
- [27] A. Motallebzadeh, N.S. Peighambardoust, S. Sheikh, H. Murakami, S. Guo, D. Canadinc, Microstructural, mechanical and electrochemical characterization of TiZrTaHfNb and Ti<sub>1.5</sub>ZrTa<sub>0.5</sub>Hf<sub>0.5</sub>Nb<sub>0.5</sub> refractory high-entropy alloys for biomedical applications, Intermetallics 113 (2019) 106572.

- [28] Y.D. Wu, Y.H. Cai, T. Wang, J.J. Si, J. Zhu, Y.D. Wang, X.D. Hui, A refractory Hf<sub>25</sub>Nb<sub>25</sub>Ti<sub>25</sub>Zr<sub>25</sub> high-entropy alloy with excellent structural stability and tensile properties, Mater. Lett. 130 (2014) 277–280.
- [29] Y. Iijima, T. Nagase, A. Matsugaki, P. Wang, K. Ameyama, T. Nakano, Design and development of Ti–Zr–Hf–Nb–Ta–Mo high-entropy alloys for metallic biomaterials, Mater. Des. 202 (2021) 109548.
- [30] W. Yang, Y. Liu, S.J. Pang, P.K. Liaw, T. Zhang, Bio-corrosion behavior and in vitro biocompatibility of equimolar TiZrHfNbTa high-entropy alloy, Intermetallics 124 (2020) 106845.
- [31] Y. Ma, Q. Wang, B.B. Jiang, C.L. Li, J.M. Hao, X.N. Li, C. Dong, T.G. Nieh, Controlled formation of coherent cuboidal nanoprecipitates in body-centered cubic high-entropy alloys based on Al<sub>2</sub>(Ni,Co,Fe,Cr)<sub>14</sub> compositions, Acta Mater. 147 (2018) 213–225.
- [32] Y. Ma, Q. Wang, C. Li, L.J. Santodonato, M. Feygenson, C. Dong, P.K. Liaw, Chemical short-range orders and the induced structural transition in high-entropy alloys, Scripta Mater. 144 (2018) 64–68.
- [33] Y. Guo, X. Li, Q. Liu, A novel biomedical high-entropy alloy and its laser-clad coating designed by a cluster-plus-glue-atom model, Mater. Des. 196 (2020) 109085
- [34] Q. Wang, C. Ji, Y. Wang, J. Qiang, C. Dong, β-Ti alloys with low young's moduli interpreted by cluster-plus-glue-atom model, Metall. Mater. Trans. 44 (2013) 1872–1879.
- [35] C. Pang, B. Jiang, Y. Shi, Q. Wang, C. Dong, Cluster-plus-glue-atom model and universal composition formulas [cluster](glue atom)<sub>x</sub> for BCC solid solution alloys, J. Alloys Compd. 652 (2015) 63–69.
- [36] J. Friedel, Electronic structure of primary solid solutions in metals, Adv. Phys. 50 (2001) 539–595.
- [37] A. Takeuchi, A. Inoue, Calculations of mixing enthalpy and mismatch entropy for ternary amorphous alloys, Mater. Trans., JIM 41 (2000) 1372–1378.
- [38] T. Nagase, Y. Iijima, A. Matsugaki, K. Ameyama, T. Nakano, Design and fabrication of Ti–Zr-Hf-Cr-Mo and Ti–Zr-Hf-Co-Cr-Mo high-entropy alloys as metallic biomaterials, Mater. Sci. Eng. C 107 (2020) 110322.
- [39] S. Wang, D. Wu, H. She, M. Wu, D. Shu, A. Dong, H. Lai, B. Sun, Design of high-ductile medium entropy alloys for dental implants, Mater. Sci. Eng. C 113 (2020) 110959.
- [40] P.J. Bania, Beta titanium alloys and their role in the titanium industry, JOM 46 (1994) 16-19.
- [41] M.K. Wang, J.H. Yuan, F.Y. Yu, Q. Wang, Y.F. Liu, Z.W. Zhang, C. Dong, P.K. Liaw, Formation and mechanical behavior of body-centered-cubic Zr(Hf)-Nb-Ti mediumentropy alloys, Metall. Mater. Trans. 52 (2021) 2100–2110.
- [42] S.J. Pang, Y. Liu, H.F. Li, L. Sun, Y. Li, T. Zhang, New Ti-based Ti-Cu-Zr-Fe-Sn-Si-Ag bulk metallic glass for biomedical applications, J. Alloys Compd. 625 (2015) 323–327.
- [43] Y. Liu, S.J. Pang, H.F. Li, Q. Hu, B. Chen, T. Zhang, Formation and properties of Ti-based Ti–Zr–Cu–Fe–Sn–Si bulk metallic glasses with different (Ti+Zr)/Cu ratios for biomedical application, Intermetallics 72 (2016) 36–43.
- [44] W.C. Oliver, G.M. Pharr, An improved technique for determining hardness and elastic modulus using load and displacement sensing indentation experiments, J. Mater. Res. 7 (1992) 1564–1583.
- [45] BS EN ISO 14577-1, Metallic Materials Instrumented Indentation Test for Hardness and Materials Parameters - Part 1: Test Method, 2016.
- [46] J.G. Swadener, E.P. George, G.M. Pharr, The correlation of the indentation size effect measured with indenters of various shapes, J. Mech. Phys. Solid. 50 (2002) 681–694.
- [47] Q.-T. Song, J. Xu, (TiZrNbTa)<sub>90</sub>Mo<sub>10</sub> high-entropy alloy: electrochemical behavior and passive film characterization under exposure to Ringer's solution, Corrosion Sci. 167 (2020) 108513.
- [48] Q. Wang, Q. Li, X. Li, R. Zhang, X. Gao, C. Dong, P.K. Liaw, Microstructures and stability origins of β-(Ti,Zr)- (Mo,Sn)-Nb alloys with low Young's modulus, Metall. Mater. Trans. 46 (2015) 3924–3931.
- [49] K. Ishida, Schaeffler-Type phase diagram of Ti-based alloys, Metall. Mater. Trans. 48 (2017) 4990–4998.
- [50] S. Guo, C. Ng, J. Lu, C.T. Liu, Effect of valence electron concentration on stability of fcc or bcc phase in high entropy alloys, J. Appl. Phys. 109 (2011) 103505.
- [51] H. Ikehata, N. Nagasako, T. Furuta, A. Fukumoto, K. Miwa, T. Saito, First-principles calculations for development of low elastic modulus Ti alloys, Phys. Rev. B 70 (2004) 174113.
- [52] G. Grimvall, Thermophysical Properties of Materials, Elsevier Science B.V, 1999, pp. 27–45.
- [53] S. Guo, Y. Shang, J. Zhang, J. Zhang, Q. Meng, X. Cheng, X. Zhao, A metastable β-type Zr-4Mo-4Sn alloy with low cost, low Young's modulus and low magnetic susceptibility for biomedical applications, J. Alloys Compd. 754 (2018) 232–237.
- [54] K.S. Chan, A computational approach to designing ductile Nb-Ti-Cr-Al solidsolution alloys, Metall. Mater. Trans. 32 (2001) 2475–2487.
- [55] A. Leyland, A. Matthews, On the significance of the H/E ratio in wear control: a nanocomposite coating approach to optimised tribological behaviour, Wear 246 (2000) 1–11.
- [56] Y. Tanaka, M. Nakai, T. Akahori, M. Niinomi, Y. Tsutsumi, H. Doi, T. Hanawa, Characterization of air-formed surface oxide film on Ti–29Nb–13Ta–4.6Zr alloy surface using XPS and AES, Corrosion Sci. 50 (2008) 2111–2116.
- [57] C. Vasilescu, S.I. Drob, J.M. Calderon Moreno, P. Osiceanu, M. Popa, E. Vasilescu, M. Marcu, P. Drob, Long-term corrosion resistance of new Ti-Ta-Zr alloy in

- simulated physiological fluids by electrochemical and surface analysis methods, Corrosion Sci. 93 (2015) 310–323.
- [58] H. Matsuno, A. Yokoyama, F. Watari, M. Uo, T. Kawasaki, Biocompatibility and osteogenesis of refractory metal implants, titanium, hafnium, niobium, tantalum and rhenium, Biomaterials 22 (2001) 1253–1262.
- [59] J. Li, S.J. Li, Y.L. Hao, H.H. Huang, Y. Bai, Y.Q. Hao, Z. Guo, J.Q. Xue, R. Yang, Electrochemical and surface analyses of nanostructured Ti–24Nb–4Zr–8Sn alloys in simulated body solution, Acta Biomater. 10 (2014) 2866–2875.